Surfaces and Interfaces 53 (2024) 105097

Contents lists available at ScienceDirect

Surfaces and Interfaces

journal homepage: www.sciencedirect.com/journal/surfaces-and-interfaces

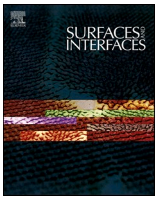

Metal-enhanced carbon-nitrogen material for selective detection of hazardous gases: Insights from interface electronic states

Mingyang Gu [a], Lin Tao [a,*], Davoud Dastan [b], Jie Dang [c], Xueyuan Zhang [d], Lixiang Li [a], Baigang An [a,*]

[a] School of Chemical Engineering, University of Science and Technology Liaoning, Anshan 114051, China
[b] Department of Materials Science and Engineering, Cornell University, Ithaca, NY 14850, United States
[c] College of Materials Science and Engineering, Chongqing University, Chongqing 400044, China
[d] Institute of Corrosion Science and Technology, Guangzhou 510530, China

ARTICLE INFO

Keywords:
Gas-sensitive
Electronic states
Thermal runaway
DFT calculation
Selectivity

ABSTRACT

In this study, utilizing density functional theory, the C_3N_1 monolayer modified by Ir, Pd, Pt, and Rh atoms (Ir/Pd/Pt/Rh-C_2N_1) was chosen for selective adsorption of C_2H_2 amidst multiple gases (H_2O, C_2H_2, and $C_4H_{10}O_2$). According to the results of cohesive energy and *ab initio* molecular dynamics simulations, it is indicated that precious metal atoms can be stably anchored on the monolayer while enhancing the conductivity of the material The analysis of the electrostatic potential and work function determined the highly active sites and electron release capacity. In addition, the adsorption energy and distance disclosed the gas-solid interface structure of multiple gases on the Ir/Pd/Pt/Rh-C_2N_1 monolayer. Importantly, C_2H_2 exhibits strong responses to p-type semiconductor Pt-C_2N_1 and n-type semiconductor Ir-C_2N_1, respectively. Crystal Orbital Hamilton Population reveals the difference in adsorption energy due to modifications involving four precious metals. Interestingly, for the first time, the density of states calculation reveals that under the coexistence of multiple gases, the Pt/Ir-C_2N_1 monolayer effectively eliminates the interference of other gases and has a unique response only to C_2H_2. In real situations, with the basis of Gibbs free energy and Einstein's law of diffusion, it was determined that Pt-C_2N_1 and Ir-C_2N_1 showed excellent hydrophobicity, a wider temperature range, and a low diffusion activation energy barrier. In summary, Pt-C_2N_1 and Ir-C_2N_1 detect C_2H_2 without interference, maintaining fundamental principles, responsiveness, stability, and versatility unaffected by external factors.

1. Introduction

With the widespread adoption of batteries, their safety has garnered considerable attention [1-5]. Thermal runaway in batteries, often triggered by aging or improper use, can lead to increased internal pressure and volume expansion, culminating in combustion and explosion. Given the complex composition of electrolytes, battery thermal runaway can release various harmful gases, including acetylene (C_2H_2) and other flammable substances [6-10]. Leaks of these gases may cause equipment corrosion, short circuits, and even explosions. Thus, monitoring battery stability and developing sensors capable of rapidly detecting gases emitted during battery instability are paramount. Early detection of vaporization products from battery thermal instability, such as those released by dimethyl carbonate ($C_4H_{10}O_2$) [1] and C_2H_2 [11], is essential for sensors capable of issuing warnings to the battery management system, disconnecting the battery from the system to prevent damage or explosion.

At present, there are a large number of two-dimensional (2D) nanomaterials. The reason is that they have a very large specific surface area, thermal conductivity, excellent photoelectric characteristics and catalytic activity, thereby showing a very significant ability in gas sensing [12-17], such as the Sc_2CO_2 monolayer [18] and graphene [19]. Nevertheless, inherent drawbacks of 2D nanosheets, including low stability and excessive adsorption capacity, have constrained their practical utility in gas sensing materials [20-23]. Hence, the exploration of high-performance gas sensors is of paramount importance. As gas-sensitive materials, the shape, structure, and doping transition metal (TM) atoms of 2D nanomaterials significantly influence sensor performance [24-26]. Modification through metal atoms doping has been pursued to enhance sensor performance [27-32]. Studies have revealed

---

* Corresponding authors at: School of Chemical Engineering, University of Science and Technology Liaoning, Anshan 114051, China.
E-mail addresses: taolin@ustl.edu.cn (L. Tao), bgan@ustl.edu.cn (B. An).

https://doi.org/10.1016/j.surfin.2024.105097
Received 12 August 2024; Received in revised form 7 September 2024; Accepted 11 September 2024

that incorporating mixed transition precious metal atoms into 2D basal materials effectively enhances sensor performance, demonstrating promising potential in the field of gas sensing [33-35].

The density functional theory (DFT) calculation method integrates advanced approaches, including first-principles calculations and ab initio molecular dynamics simulations. This method enables more accurate and comprehensive predictions of factors influencing two-dimensional material perception efficiency. By examining monolayer materials [36-40], it allows for an in-depth and exhaustive elucidation of the intrinsic principles and mechanisms governing the material perception process at the microscopic level. A novel two-dimensional layered C_3N was theoretically designed through computational simulations, investigate its intrinsic properties [41-44]. In the field of gas sensors, the C_3N framework has broad application prospects and can serve as a good carrier of precious metals, showing excellent performance in gas capture. [45-49]. As a chemical gas sensor, the C_3N single layer exhibits richness, low cost, and ease of manufacture, playing a significant role in sensor technology.

Previous research has combined experiments with complex computational studies on assess the suitability of precious structures doped with metal for uses of sensors [50-53]. These research efforts have provided visual insights into the gas sensing properties and thoroughly characterized the sorption properties of the gas detecting devices, enhancing their feasible applicability. The electrical response was generated on the sensing monolayer due to the cumulative effect of various gases. However, the current problem is that the existing technology is difficult to distinguish the contributions made by each gas. In the case where multiple gases are adsorbed together, in order to improve selectivity, the interference of electrical signals generated by redundant gases needs to be eliminated on the premise of only focusing on specific gases.

In this study, the responses of monolayers prepared with precious metals (Ir, Pd, Pt, and Rh) under various gases (H_2O, C_2H_2, and $C_4H_{10}O_2$) were calculated using the DFT method. The stability and rationality of the monolayer were confirmed from multiple perspectives such as bond length, cohesive energy, and *ab initio* molecular dynamics. The gas adsorption mechanism was clarified by calculating the Crystal Orbital Hamilton Population (COHP). The selective electrical response behavior generated during gas adsorption was evaluated by using the density of states (DOS) method. The calculations of Gibbs free energy and diffusion energy barrier can understand the thermodynamic feasibility and spontaneity of related reactions or processes and the difficulty degree of substance diffusion, which is very important for understanding the response speed and sensitivity of the sensor. Our research provides a new perspective for improving the selectivity of sensors.

2. Experimental method

Employing DFT via the Dmol^3 [54], we performed a thorough structural and electronic assessment on the TM-C_2N_1 monolayer and gas molecules. Utilizing the Perdew-Burke-Ernzerhof functional along with gradient-corrected approximation for correlation [55,56]. A double precision number basis set polarization function is utilized to handle atomic orbitals. The dispersion-corrected DFT method was chosen based on Grimme vdW correction [57], which can accurately describe the interaction in all weak calculations. The global cut-off radius of the real space reaches 4.9 Å. K-point sampling of the Brillouin zone, executed via the Monkhorst-Pack scheme with a 3 × 3 × 1 mesh, facilitated a theoretical analysis. Geometry optimization was refined with convergence criteria set to 1×10^{-5} Ha for energy, 0.002 Ha/Å for atomic forces, and 0.005 Å for displacement. The electron distribution and charge transfer were computed by using the Mulliken method [58]. A 20 Å vacuum layer is perpendicularly applied to the Pt/Pd/Ir/Rh-C_2N_1 monolayer to prevent interactions between periodic structures.

3. Results and discussions

3.1. Structural characterizations

The optimized structure of the Pt/Ir/Pd/Rh-C_2N_1 monolayer is depicted in Fig. 1**a**. It provides the top sight of the modified point of the precious metal-to-C_2N_1 monolayer and a main view of the modified TM-C_2N_1 monolayer. Clearly, based on earlier research observations [48, 59], the four doped precious metals are placed on the top of the 2D material, giving rise to the most stable configuration. By studying the different charge density distributions shown in Fig. 1**b**, we can gain a deeper understanding of how the doping of precious metal atoms affects the stability of monolayer materials. The dark red color significantly increases around the C and N atoms on the material surface, indicating a significant increase in the charge density of the electron wave function on the material surface, further confirming that the surface after metal doping has an excellent charge acceptance. The electron transfer process is governed by the valence electron configuration and Fermi energy levels of these metals. Therefore, after doping with precious metals, in order to ensure the stability of the structure, the precious metal atoms will protrude from the monolayer and be located at the top of the structure, resulting in structural deformation. This positioning leads to substantial substrate deformation, thereby inducing alterations in the electronic band structure and mechanical stress distribution of the entire system.

For the anchoring situation of precious metal atoms on the monolayer, this study analyzes it through cohesive energy (E_{coh}). At the outset, the E_{coh} was defined as [60,61]:

$$E_{coh} = \frac{(n_1 E_{TM} + n_2 E_C + n_3 E_N - E_{C_2N_1})}{(n_1 + n_2 + n_3)} \tag{1}$$

here, E_{TM} represents the energy (eV) of precious metal atoms such as Pt, Ir, Pd, and Rh. Different precious metal atoms may have different E_{TM} values, which depend on their respective electronic structures and nuclear characteristics. E_C represents the energy (eV) of carbon (C) atoms, which reflects the energy state of carbon in a specific environment or system. E_N is the energy (eV) of nitrogen (N) atoms, which also reflects the energy characteristics of nitrogen atoms. And n_1, n_2, and n_3 are the numbers of TM, C, and N atoms, respectively. Through the combination of these numbers and the energy values of their respective atoms (E_{TM}, E_C, and E_N), various energy-related calculations and analyses can be carried out. It was calculated that the E_{coh} of the initial C_3N_1 monolayer was 7.01 eV. After precious metal doping, the E_{coh} reduced to 6.75 eV for Ir-C_2N_1, 6.75 eV for Rh-C_2N_1, 6.70 eV for Pd-C_2N_1, and 6.70 eV for Pt-C_2N_1, a change of 4 % is within the allowable range. This indicates a robust interaction between the noble metal and the monolayer, ensuring stable binding.

The *ab initio* molecular dynamics simulations, rooted in quantum mechanics, provide a precise depiction of molecular and atomic movements and interactions. With a simulation comprising 5000 steps, each representing a 10 fs time interval, the total simulated timeframe spans 50 ps. This meticulous approach facilitates a comprehensive analysis of the structure's dynamic stability. The findings confirm the stability of the monolayer structure upon doping with precious metals, as depicted in **Figure S1**.

Analyzing the active sites and electron transport capabilities of materials for achieving the optimal performance of materials is a crucial step in the field of best-in-class gas sensing. As shown in **Figure S2**, the electrostatic potential is a physical quantity used to describe the charge distribution and electric field strength on the material surface. A higher electrostatic potential corresponds to a stronger electric field at that position, which will trigger more charge accumulation or a more active charge transfer process. The work function is the energy difference between the vacuum level and the Fermi level. For materials with a larger work function, electrons need to overcome a higher energy barrier to

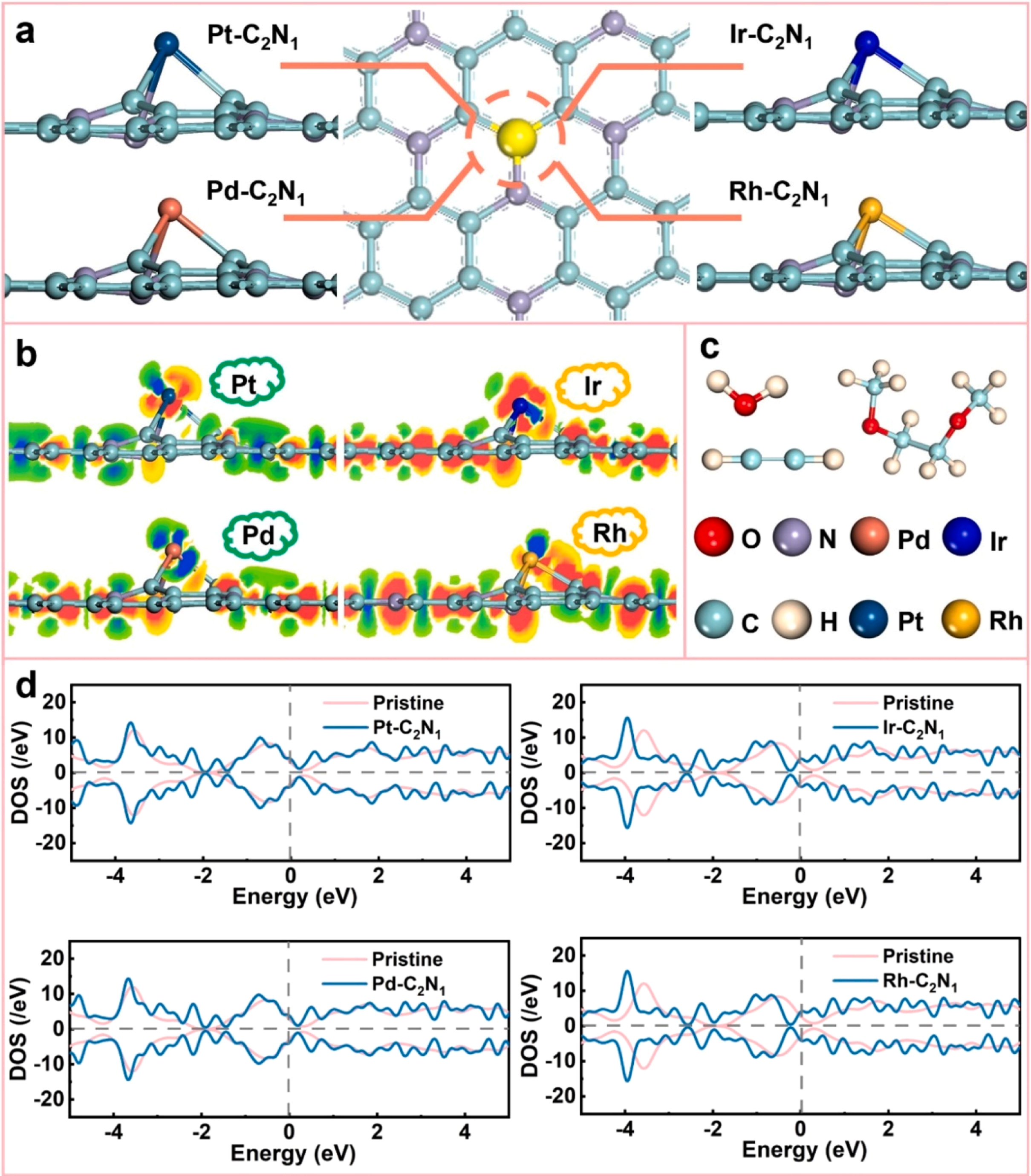

Fig. 1. (a) Configuration of the Pd/Ir/Pt/Rh-C_2N_1 monolayer. (b) Stable structure and charge density distribution of the TM-C_2N_1. (c) Structure of H_2O, C_2H_2, and $C_4H_{10}O_2$. (d) DOS of the TM-C_2N_1.

escape from the material into a vacuum. The results indicate that Pt-C_2N_1 (3.70 eV), Pd-C_2N_1 (3.70 eV), Ir-C_2N_1 (3.46 eV), and Rh-C_2N_1 (3.43 eV) exhibit comparable electron migration capabilities, suggesting similar electronic properties among these catalysts.

Fig. 1**c** it mainly describes the optimal structures of three molecules and the bond lengths of some of their bonds. For the H_2O molecule, the H—O bond length is 0.98 Å. The bond length data reflects the distance and interaction strength between hydrogen atoms and oxygen atoms. In the C_2H_2 molecule, the C—H bond length is 1.07 Å, and the C—C bond length is 1.21 Å. The shorter C—C bond length indicates a strong double bond effect between carbon and carbon, and the C—H bond length also reflects the specific interaction between carbon and hydrogen. In the $C_4H_{10}O_2$ molecule, the C—H bond length is 1.10 Å, the C—C bond length is 1.53 Å, and the C—O bond length is 1.42 Å. Different bond lengths reflect the bonding nature and interaction degree between different atoms. The longer C—C single bond has a significant difference from the double bond length, and the C—O bond length reflects the specific covalent bond characteristics between carbon and oxygen. The data obtained through calculation in this paper agree with the previous data [11], suggesting that the chosen calculation parameters are rational and precise.

According to previous studies [62-66], the electrical conductivity characteristics of a substance are reflected at the Fermi level of the DOS curve, which is associated with the electronic states at the Fermi level.

Consequently, this study adopted this method to evaluate the effect of the introduction of doped precious metals on the conductivity of materials. In Fig. 1**d**, due to the doping of precious metals, the conductivity of the material surface is enhanced, causing a change in the DOS curve and presenting an upward trend at the Fermi level. The position of the Fermi level in the DOS curve is indeed a key factor in determining the type of material. When the Fermi level is within the valence band, it means that the concentration of holes in the material is relatively high, thus showing a p-type semiconductor.

The d orbitals of noble metal atoms and the p orbitals of non-metallic C/N in the monolayer play a role in bonding. The characteristics of the d orbitals enable them to form strong chemical bonds when overlapping with other atomic orbitals. The d orbitals of noble metals have a partially filled electronic structure, which enables them to have effective interactions with the orbitals of other atoms, thereby affecting the properties and reactivity of substances. For the p orbitals of non-metallic C/N, they can also participate in the formation of chemical bonds. The shape and directionality of the p orbitals enable them to overlap with other p orbitals or d orbitals, thereby forming covalent bonds or coordination bonds.

According to the results, among these materials, there is an obvious alignment effect between the d orbitals of Pd and Rh and the p orbitals of C/N, which means that the electronic interaction between them is relatively strong. This will affect their selectivity because the transfer of electrons and the progress of the reaction are related to the position of the energy level and the degree of hybridization. In addition, the hybridization of the d orbitals of Pt and Ir with the p orbitals of C/N is more significant and is located at a higher energy level. Specifically, a higher energy level may lead to differences in their adsorption and activation abilities for reactants, thereby affecting the rate and selectivity of the reaction. The results showed that Pt, Pd, Ir, and Rh could be firmly attached to the C_2N_1 monolayer.

3.2. Gas sensing performance

3.2.1. Gas adsorption behavior

Herein this section, the preliminary determination of the optimal gas adsorption configuration is made. Then, quantitative analysis was conducted on the adsorption energy and distance. Eventually, the difference regarding the performance of gas adsorption is clarified with the application of COHP. The configurations of each adsorption site are shown in **Figure S4-S15**, and different locations of gas adsorption combined with configurations were investigated on Pt-C_2N_1, Pd-C_2N_1, Rh-C_2N_1, and Ir-C_2N_1. Initially, each gas molecule, positioned at a height of 2.5 Å from the monolayer, undergoes structural optimization to establish its equilibrium state. On the basis of the positive relationship involving the distance of adsorption and energy, the initial configuration that complied with this criterion was picked [67,68], as shown in **Figure S16-S18**. Fig. 2 presents the most steadfast adsorption patterns and the charge densities related to the three gases at Pt-C_2N_1, Pd-C_2N_1,

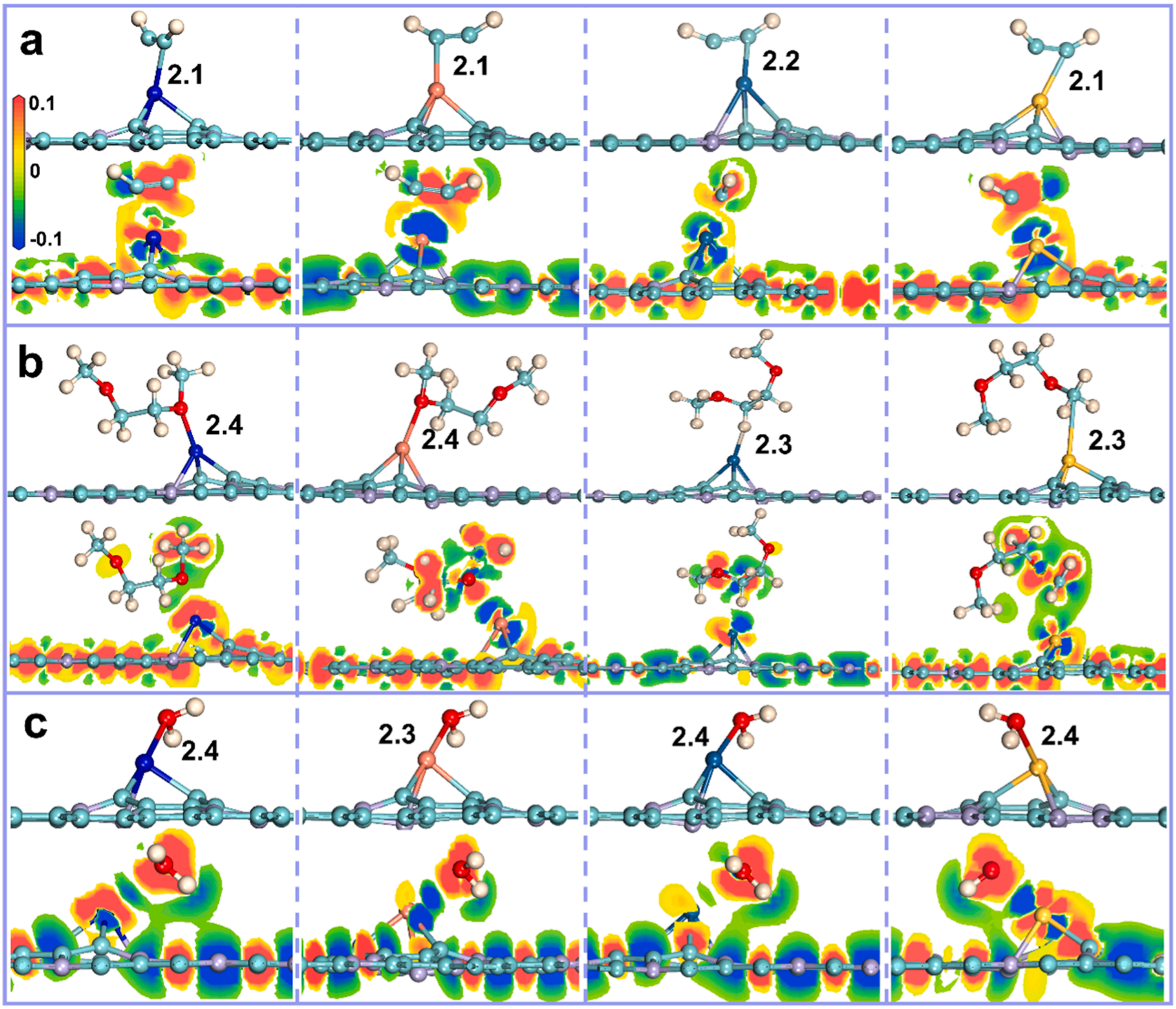

Fig. 2. Stable configuration and charge density distribution of gas on the Ir-C_2N_1, Pd-C_2N_1, Pt-C_2N_1, and Rh-C_2N_1 monolayer. (a) C_2H_2, (b) $C_4H_{10}O_2$, and (c) H_2O.

$Rh\text{-}C_2N_1$ and $Ir\text{-}C_2N_1$.

Fig. 2 reveals the least atomic distances that were observed on the surfaces of $Ir\text{-}C_2N_1$, $Pd\text{-}C_2N_1$, $Pt\text{-}C_2N_1$, and $Rh\text{-}C_2N_1$ for different gas molecules. Specifically, for C_2H_2 molecules, the adsorption distances on the $Ir\text{-}C_2N_1$, $Pd\text{-}C_2N_1$, $Pt\text{-}C_2N_1$, and $Rh\text{-}C_2N_1$ surfaces are 2.1 Å, 2.1 Å, 2.2 Å, and 2.1 Å, respectively. For $C_4H_{10}O_2$ molecules, the adsorption distances on the $Ir\text{-}C_2N_1$, $Pd\text{-}C_2N_1$, $Pt\text{-}C_2N_1$, and $Rh\text{-}C_2N_1$ surfaces are 2.4 Å, 2.4 Å, 2.3 Å, and 2.3 Å, respectively. Lastly, for H_2O molecules, the adsorption distances on the $Ir\text{-}C_2N_1$, $Pd\text{-}C_2N_1$, $Pt\text{-}C_2N_1$, and $Rh\text{-}C_2N_1$ surfaces are 2.4 Å, 2.3 Å, 2.4 Å, and 2.4 Å, respectively.

After optimization, the C_2H_2 adsorption on $Ir/Pd/Pt/Rh\text{-}C_2N_1$ results in shorter atomic distances than $C_4H_{10}O_2$ and H_2O, consistently. In addition, the charge density was analyzed to examine the charge build-up and depletion throughout the interaction of the gas with $Ir/Pd/Pt/Rh\text{-}C_2N_1$ more visually, and the results are shown in Fig. 2. Refer to **Table S1** for specific charge transfer values. The charge density of the electron wave function indicates that $Ir/Pd/Pt/Rh\text{-}C_2N_1$ will deliver a large amount of charge during the process of gas adsorption. It is evident that the regions adjacent to the gas molecules exhibit a dark red hue, signifying electron transfer from $Pt\text{-}C_2N_1$, $Pd\text{-}C_2N_1$, $Rh\text{-}C_2N_1$, and $Ir\text{-}C_2N_1$ to the gas molecules. This observation indicates a robust interaction between the gases and the C_2N_1 complexes, underscoring the significant role of Ir, Pd, Pt, and Rh in this electron exchange process. The results demonstrate significant charge transfer to C_2H_2 on all four surfaces, indicating that $TM\text{-}C_2N_1$ exhibits strong adsorption effects on C_2H_2. This effect is particularly pronounced on the $Pt\text{-}C_2N_1$ and $Ir\text{-}C_2N_1$ monolayers.

Fig. 3**a** shows the adsorption behavior of the gas more comprehensively by comparing the adsorption energy and the adsorption distance, and quantitatively evaluates the interaction force between the gas and $Ir/Pd/Pt/Rh\text{-}C_2N_1$. Adsorption energy is specified as [64]:

$$E_{ads} = E_{total} - \left(E_{\text{monolayer}} + E_{gas}\right) \tag{2}$$

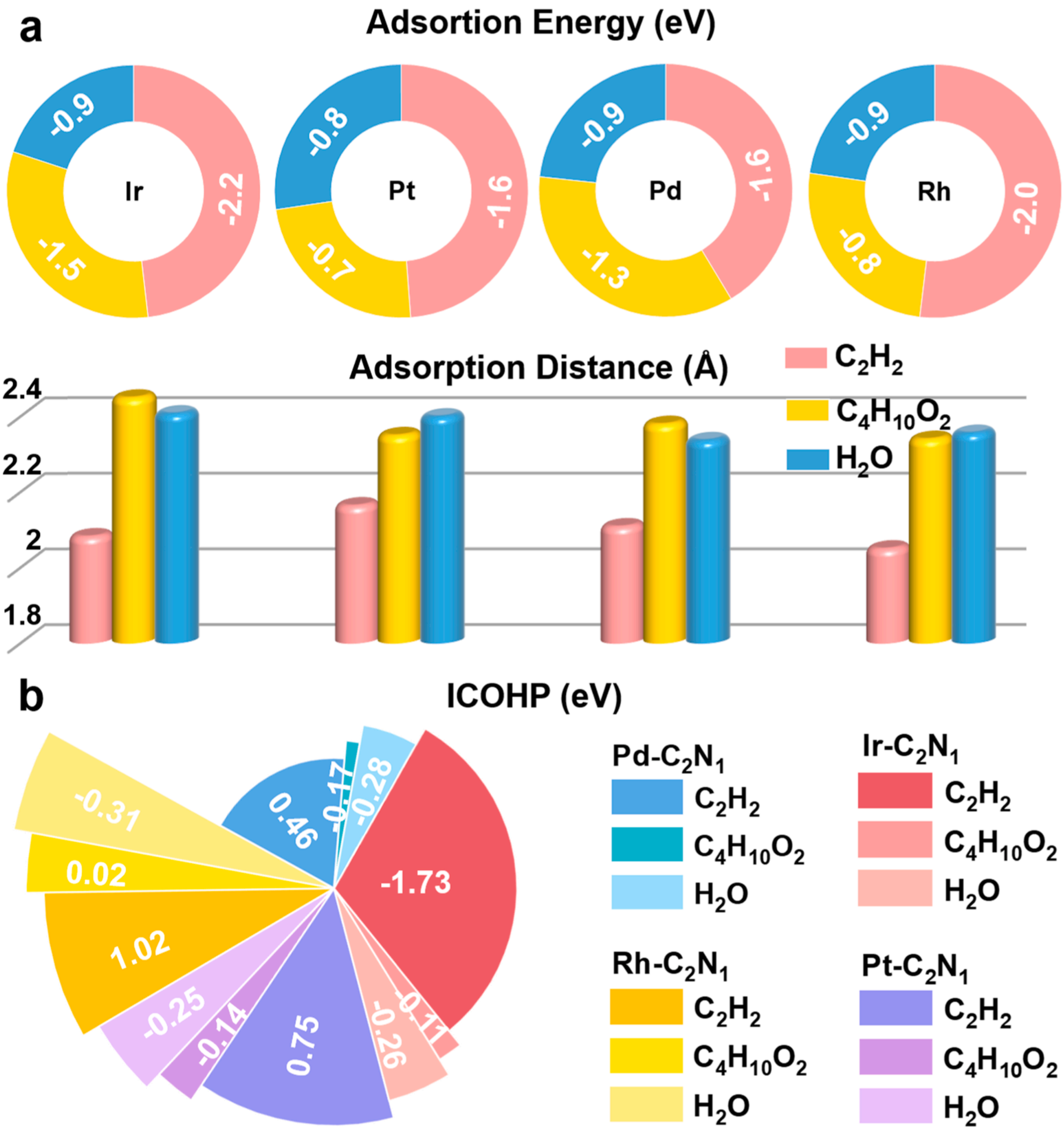

Fig. 3. (a) Adsorption energy and distance of gases on $TM\text{-}C_2N_1$. (b) ICOHP value of gases on $TM\text{-}C_2N_1$.

where E_{ads} represents the adsorption energy (eV), E_{total} the total energy that the gas has after adsorption on the monolayer (eV), $E_{monolayer}$ the energy that the two-dimensional monolayer has before gas adsorption (eV), and E_{gas} the energy of the gas alone (eV).

Fig. 3**a** shows from the perspective of adsorption energy that the adsorption energy of C_2H_2 is much stronger than that of the other two gases, much stronger than that of $C_4H_{10}O_2$ and H_2O. This phenomenon indicates that C_2H_2 gas can achieve selective adsorption of monolayers in a multi-gas environment, regardless of the occurrence of other gases. Additionally, it is worthy of note that the energy of H_2O adsorption on the TM-C_2N_1 is weak., indicating that Pt-C_2N_1, Pd-C_2N_1, Rh-C_2N_1, and Ir-C_2N_1 have almost no adsorption effect on H_2O. Therefore, a humid environment does not affect the performance of Pt-C_2N_1, Pd-C_2N_1, and Ir-C_2N_1. On the whole, the adsorption distance of C_2H_2 was the smallest and the adsorption distance of H_2O and $C_4H_{10}O_2$ was the largest, indicating that the Ir/Pd/Pt/Rh-C_2N_1 monolayer had the best adsorption performance for C_2H_2 gas among the three gases, and the most prominent ones were Pd-C_2N_1 and Ir-C_2N_1.

It can be observed that the adsorption functions of the surfaces doped with four different precious metals for C_2H_2 exceed those of $C_4H_{10}O_2$ and H_2O. Take for example, the energy of adsorption of Pt-C_2N_1—C_2H_2 is −1.6 eV, which is stronger than the adsorption energy of Pt-C_2N_1—$C_4H_{10}O_2$ of −0.7 eV and the adsorption energy of Pt-C_2N_1—H_2O of −0.8 eV. In order to reveal the difference in the adsorption energy of Pt-C_2N_1, Pd-C_2N_1, Rh-C_2N_1, and Ir-C_2N_1 from the perspective of chemical bonding, the chemical bonds were divided into bonding bonds and antibonds, in which bonding played a decisive role. COHP analysis was employed to examine the interatomic forces in the process of gas adsorption more accurately. **Figures S19-S22** is the result of the calculation. To obtain an accurate explanation, the integral COHP (ICOHP) values were calculated, this means that when the ICOHP value is more negative, the bonding between noble metal atoms and gas atoms is tighter and the interaction is stronger. This calculation and analysis are helpful for an in-depth understanding of the properties and reaction mechanisms of the materials, providing valuable information for further research and applications. In Fig. 3**b**, of all the gas molecules, C_2H_2 presents the most remarkable ICOHP value on the Ir/Pt-C_2N_1 surface.

3.2.2. *Electrical response behavior*

The above results demonstrate the preferential adsorption behavior of C_2H_2 on the surfaces of the two materials (Ir/Pt-C_2N_1). To further verify whether these two promising candidate gas-sensitive materials can be utilized for the selective electrical response to C_2H_2, we investigated its electrical response behavior. From the perspective of gas adsorption, the adsorption of C_2H_2 in the four surface systems exhibits distinct characteristics. To identify suitable sensing materials, conductivity analysis was conducted based on the DOS to select materials with the most favorable electrical response to C_2H_2.

Selectivity is paramount for gas sensors. Building upon prior research [62-64], the fluctuations of the Fermi level DOS curve can provide an in-depth understanding of the internal mechanism of the change in the conductivity of materials and provide a theoretical basis for the design and optimization of materials. The Fermi level is an important physical concept, which represents the dividing line between the occupied and

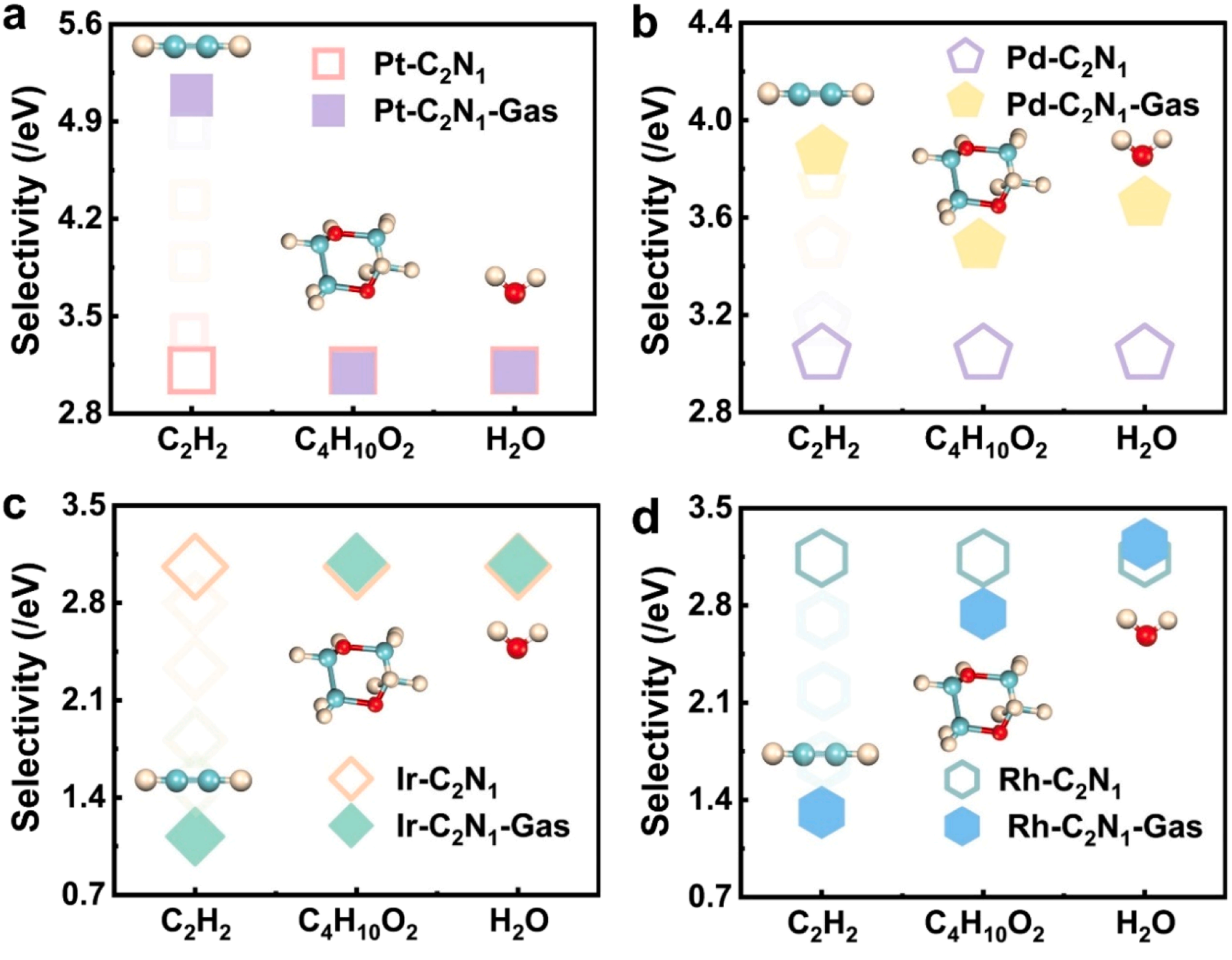

Fig. 4. Selectivity of gases on the (a) Pt-C_2N_1, (b) Pd-C_2N_1, (c) Ir-C_2N_1, and (d) Rh-C_2N_1 monolayer.

unoccupied energy levels of electrons at absolute zero. When the conductivity of the material changes, it means that the transmission characteristics of electrons in the material have changed, affecting the energy state distribution of electrons. This change will have an impact on the energy state distribution of electrons, and this impact will be reflected in the fluctuations of the DOS curve at the Fermi level. The differences in the electrical response of the three gases on the TM-C_2N_1 monolayer are analyzed in **Figures S23-S26**.

Fig. 4 optimizes the electrical response data to delineate the selectivity index of the surface towards various gases, highlighting the differential selectivity of 2D surfaces with distinct metal doping. This index is determined by comparing the conductivity of gases before and after adsorption. Unchanged conductivity signifies no material impact, while changes denote sensitivity to the gas. In Fig. 4**a and** 4**b**, the conductivity of C_2H_2 adsorbed on Pt-C_2N_1 and Pd-C_2N_1 surfaces significantly surpasses background conductivity, resulting in increased electron concentration near this level, thereby enhancing conductivity. In particular, in Fig. 4**a**, Pt-C_2N_1 exhibits robust conductivity to C_2H_2 with negligible changes upon adsorption of $C_4H_{10}O_2$ and H_2O, indicating selective responsiveness to C_2H_2. Conversely, in Fig. 4**b**, although Pd-C_2N_1 demonstrates conductivity to C_2H_2, it also exhibits substantial conductivity alterations upon adsorption of $C_4H_{10}O_2$ and H_2O, suggesting a lack of selective electrical response to C_2H_2.

In Fig. 4**c and d,** the Ir-C_2N_1 and Rh-C_2N_1 surfaces have a strong conductivity change after C_2H_2 adsorption. In Fig. 4**c**, after the adsorption of C_2H_2 gas on the Ir-C_2N_1 surface, its electrical conductivity changes, and the position of the Fermi level also undergoes a significant shift, but no significant change for $C_4H_{10}O_2$ and H_2O, indicating that it can achieve a selective response to C_2H_2. In Fig. 4**d**, although Rh-C_2N_1 has a certain conductivity change for C_2H_2, it also has a significant conductivity change for the adsorption of $C_4H_{10}O_2$ and H_2O, which indicates that Rh-C_2N_1 cannot achieve selective electrical response to C_2H_2. Thus, the C_2N_1 monolayer modified with precious metal atoms Pt and Ir exhibits selective response to C_2H_2 gas among other gases (C_2H_2 and H_2O). It is worth noting that the conductivity of Pt/Ir-C_2N_1 after adsorption of H_2O does not change, it indicates that the Pt/Ir-C_2N_1 monolayer is not water-affinitive.

The redistribution of charge after C_2H_2 adsorption is the main cause of conductivity change, and the analysis of DOS and PDOS is visualized in **Figures S23-S30**. The results show that the n-type semiconductor Ir-C_2N_1 and p-type semiconductor Pt-C_2N_1 have the ability to form selective electrical signal response to C_2H_2 gas and have good hydrophobicity. PDOS analysis showed that C atoms played a key role in the adsorption process of Pt/Ir/Pd/Rh-C_2N_1 gas. The **Supporting Information** contains detailed analyses.

It is significant to observe that the conductivity of H_2O adsorbed on the Pt/Ir-C_2N_1 monolayer undergoes very slight changes, as shown in Fig. 4, and no notable change was witnessed. This result confirmed that Pt/Ir-C_2N_1 can selectively detect C_2H_2 without being affected by humidity and can give a good selective electrical signal response to C_2H_2. To probe the influence of humidity on the C_2H_2 sensor's electrical response, adsorption energy and DOS calculations were performed under conditions with varying H_2O:C_2H_2 ratios. By incrementally raising H_2O levels, while holding C_2H_2 constant, this study determined the maximum humidity tolerance of the Ir/Pt-C_2N_1 sensor to C_2H_2, ensuring reliable detection without performance compromise. Fig. 5**a**

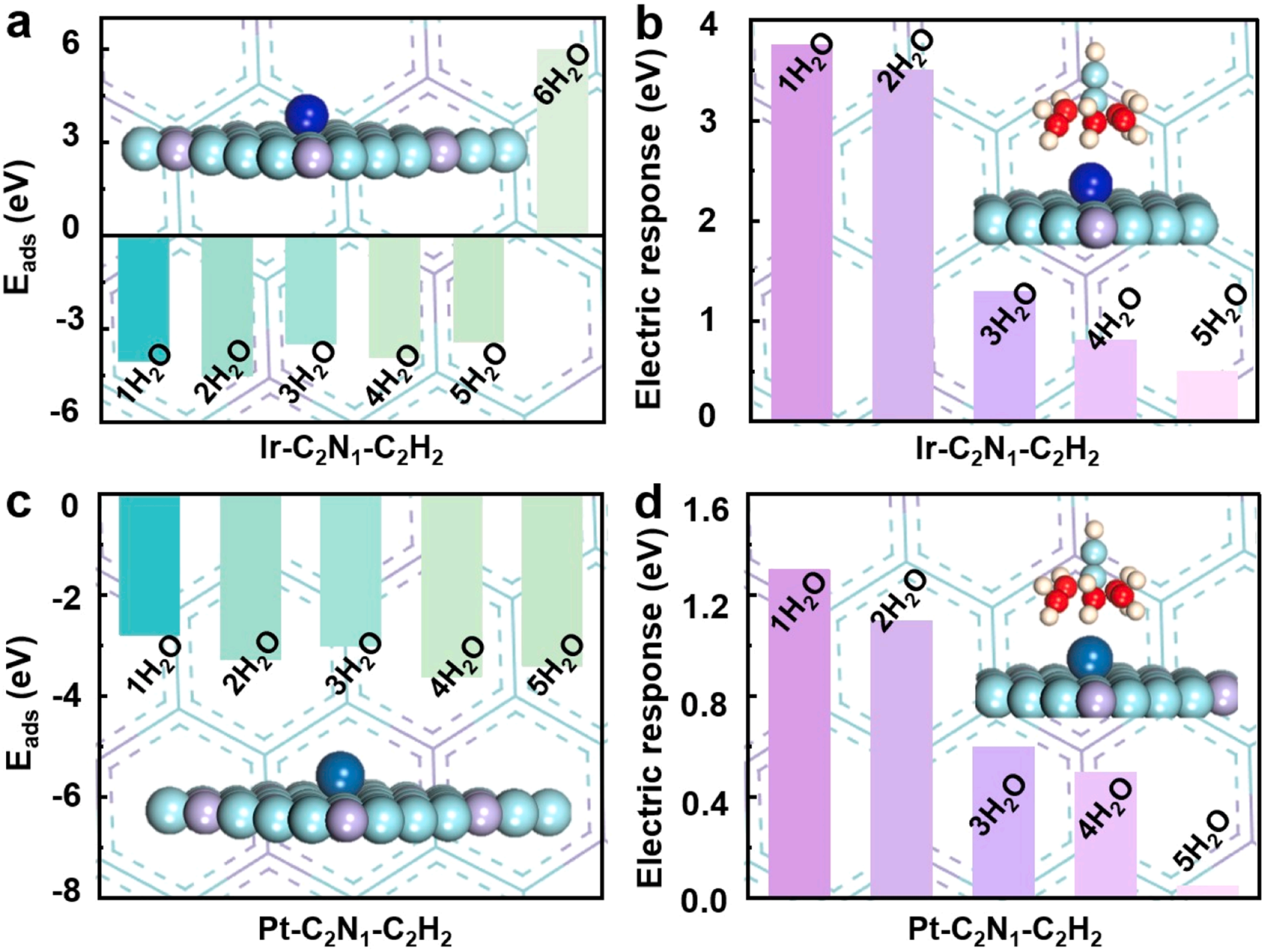

Fig. 5. Adsorption energy of different amounts of H_2O with C_2H_2 on (a) Ir-C_2N_1, (c) Pt-C_2N_1, and electrical response of C_2H_2 on (b) Ir-C_2N_1, (d) Pt-C_2N_1.

illustrates that the adsorption of six H_2O molecules on the Ir-C_2N_1 is endothermic, indicating no adsorption occurs. Consequently, Ir-C_2N_1 is capable of adsorbing C_2H_2 at its maximum capacity coexisting with five H_2O molecules. The change in the DOS at the Fermi level, as depicted in Fig. 5**b**, suggests that there is still a detectable response to C_2H_2 even in the presence of five H_2O molecules. Additionally, Fig. 5**c** demonstrates that C_2H_2 can be adsorbed onto Pt-C_2N_1 when five H_2O molecules are present. However, as shown in Fig. 5**d**, the electrical response in this case is significantly reduced, indicating that Pt-C_2N_1 is capable of generating a maximum response to C_2H_2 under this condition.

3.3. *Applications of gas sensors*

To delineate the optimal temperature range for high-performance gas sensing, this study assessed the operational milieu, with a spotlight on the gas diffusion properties of sensor materials. Molecular dynamics simulations were employed to check the diffusion profiles of three target gases. Given the temperature-dependent nature of material properties, pinpointing the temperature sweet spot for peak material performance is crucial. Calculating Gibbs free energy was fundamental to this endeavor, offering insights into the thermodynamic viability of material processes across various temperatures. This calculation is vital for ascertaining the spontaneity and extent of material-involved reactions at specific temperatures, thereby providing a robust theoretical framework for optimizing the operational temperature window. Detailed computational details are presented in the **Supporting Information**.

The propensity for spontaneous adsorption is directly correlated with the negativity of the Gibbs free energy. The Gibbs free energy at various temperatures was meticulously calculated so as to identify the temperature ranges in which the free energy remained negative, indicating spontaneous adsorption. Consequently, the practical temperature applicability for gas-sensitive materials TM-C_2N_1 was established. Fig. 6**a and c** illustrate the direct correlation concerning the Gibbs free energy for the adsorption of three distinct gases at Ir/Pt-C_2N_1 and the corresponding temperatures. The linear relationship established in **Figure S31** can be obtained through theoretical calculations. In Fig. 6, $\Delta G < 0$ is evident for the p-type semiconductor Pt-C_2N_1 at 600 K, as well as for the n-type semiconductor Ir-C_2N_1 at the same temperature. This observation suggests that Pt/Ir-C_2N_1 fails to adsorb certain gases above 600 K. **Figure S31** reveals $\Delta G < 0$ for the p-type semiconductor Pd-C_2N_1 and the n-type semiconductor Rh-C_2N_1 below 550 K, indicating that the optimal operating range for Pd/Rh-C_2N_1 is below 500 K. Therefore, Pt/Ir-C_2N_1 exhibits superior high-temperature resistance for gas adsorption compared to Pd/Rh-C_2N_1, suggesting that Pt/Ir-C_2N_1 is more effective for the selective detection of C_2H_2 in elevated temperature environments. It is worth noting that the maximum applicable temperature for Pt/Ir-C_2N_1 is 600 K, which is the upper limit of H_2O adsorption.

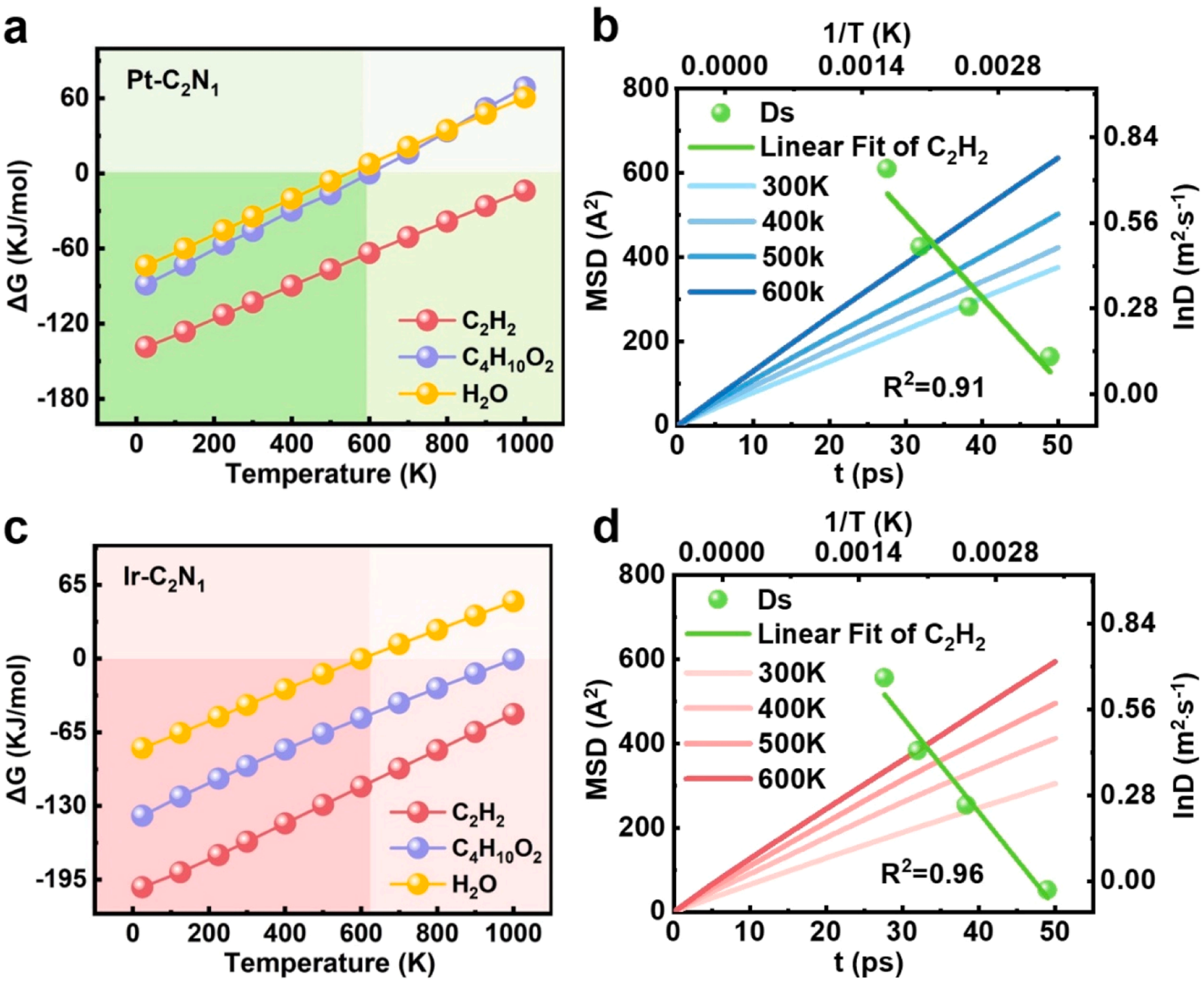

Fig. 6. Gibbs free energy of the three gases on (a) Pt-C_2N_1 and (c) Ir-C_2N_1 depending on temperature. Diffusion and mean-squared displacement of C_2H_2 on (b) Pt-C_2N_1 and (d) Ir-C_2N_1 at diverse temperatures.

Humidity does not affect selective adsorption, which is confirmed in the DOS diagram. The Pt/Ir-C_2N_1—C_2H_2 should determine the actual response temperature of Pd/Ir-C_2N_1. Temperature and humidity do not affect the response of Pt/Ir-C_2N_1 to C_2H_2. Therefore, Pt/Ir-C_2N_1 is suitable as a gas sensing material in various environments.

The study on the gas diffusion performance of various gases on the Pt/Ir-C_2N_1 material, the diffusion coefficient was computed through molecular dynamics simulation. The **Supporting Information** contains detailed calculation results. The coefficient of diffusion acts as a parameter utilized to express the diffusion capacity of a molecule. The larger the diffusion coefficient, the quicker the rate of diffusion, indicating that the lower the energy barrier necessary for the process of diffusion [69-71]. The diffusion behavior of gases is judged through the calculation results of the diffusion coefficient. **Figures S32-S35** show the stable configurations before and after the calculation. The diffusion coefficients for Pt-C_2N_1—C_2H_2 are observed to be the lowest among p-type semiconductors, while those for Ir-C_2N_1—C_2H_2 are the least within n-type semiconductors, as detailed in **Table S2**. This distinction substantiates the capability of the Pt/Ir-C_2N_1 monolayer to selectively adsorb C_2H_2 gas.

Interestingly, it is water that has the largest diffusion coefficient, indicating that the monolayer has a limited attraction for water. The diffusion rate of C_2H_2 on the monolayer is the lowest. In order to understand the C_2H_2 diffusion activation energy from a physicochemical viewpoint, the Arrhenius equation was fitted in accordance with the diffusion coefficient to attain the C_2H_2 diffusion activation energy. For detailed calculations, please refer to the **Supporting Information** and **Table S3**. The stable structure of Pt/Ir-C_2N_1—C_2H_2 at different temperatures is shown in **Figure S36 and S37**. The energy required in the adsorption process is represented by the activation energy, which has a definite influence on the difficulty of the process and the adsorption rate. As shown in Fig. 6**b and** 6**d**, the mean square displacement of C_2H_2 on Pt/Ir-C_2N_1 indicates that the diffusion activation energies of Pt-C_2N_1 and Ir-C_2N_1 are 2.6 kJ/mol and 2.7 kJ/mol, respectively. It has been confirmed that Pt-C_2N_1 holds an advantage over Pd-C_2N_1 in the detection of C_2H_2 in p-type semiconductors, and Ir-C_2N_1 has a superiority over Rh-C_2N_1 in the detection of C_2H_2 in n-type semiconductors.

The gas recovery time is one of the very important performance parameters in the practical application of sensors. When the gas is removed, the time (τ) consumed by the sensor to recover from the response state to the gas to the initial state is the response recovery time [50]. In accordance with the transition state theory, τ is calculated as:

$$\tau = A^{-1} e^{-E_a/kT} \tag{3}$$

Here, A is defined as the attempt frequency, and its value is determined to be 10^{12} per second (s^{-1}). E_a (eV) is the absolute value of adsorption energy as well as the potential barriers of desorption process. The k represents the Boltzmann constant. T represents the temperature. **Table S4-S7** provide details about the τ of three gases adsorbed on gas-sensitive materials at different temperatures. Overall, with the increase in temperature, τ decreases, which indicates a quicker desorption rate of the gas. It is necessary to point out that the Pt/Ir-C_2N_1 monolayer maintains high selectivity for C_2H_2 even in scenarios related to battery impairment and elevated gaseous temperature emissions, highlighting its superior performance.

4. Conclusions

In summary, the dispersion-corrected DFT calculation clarifies the gas sensing behavior of TM-C_2N_1. The cohesion energy and *ab initio* molecular dynamics simulations indicate the stability of the monolayer. DOS shows that Pt/Pd-C_2N_1 is a p-type semiconductor, while Ir/Rh-C_2N_1 is an n-type semiconductor. The interaction between the metal d orbitals and the p orbitals of C_2N_1 changes the electron distribution, making Pt/Ir-C_2N_1 have a high affinity for C_2H_2. This results in an obvious electrical response and reduces the interference of other gases at the same time. Pt/Ir-C_2N_1 has a wide application temperature range and is not affected by humidity. Molecular dynamics simulations provide physicochemical insights into the diffusion behavior of gases. The diffusion energy barrier of C_2H_2 is 1.1 kJ/mol for Pt-C_2N_1 and 1.0 kJ/mol for Ir-C_2N_1. The study confirms that the p-type semiconductor Pt-C_2N_1 and the n-type semiconductor Ir-C_2N_1 have obvious advantages in selective adsorption and response to C_2H_2, increasing the possibility of creating a new safety monitoring prototype.

CRediT authorship contribution statement

Mingyang Gu: Data curation, Formal analysis, Investigation, Methodology, Writing – original draft. **Lin Tao:** Validation, Data curation, Methodology, Supervision, Funding acquisition, Conceptualization, Writing – review & editing. **Davoud Dastan:** Methodology, Supervision, Resources. **Jie Dang:** Methodology, Formal analysis, Software. **Xueyuan Zhang:** Methodology, Formal analysis, Software. **Lixiang Li:** Methodology, Supervision, Resources. **Baigang An:** Supervision, Formal analysis, Writing – review & editing.

Declaration of competing interest

The authors declare that they have no known competing financial interests or personal relationships that could have appeared to influence the work reported in this paper.

Data availability

Data will be made available on request.

Acknowledgment

The funding from the National Natural Science Foundation of China (Grant No. 52304330 and 52371224), University of Science and Technology Liaoning Talent Project Grants (Grant No. 6003000317), the Outstanding Youth Fund of University of Science and Technology Liaoning (Grant No. 2023YQ11), the Youth Fund of the Education Department of Liaoning Province (Grant No. LJKQZ20222324), the Natural Science Foundation of Liaoning Province (Grant No. 2024-BS-218), and College Students' Innovative Entrepreneurial Training Plan Program (Grant No. 202410146030) are gratefully acknowledged.

Supplementary materials

Supplementary material associated with this article can be found, in the online version, at doi:10.1016/j.surfin.2024.105097.

References

[1] D. Santos-Carballal, O. Lupan, N. Magariu, N. Ababii, H. Krüger, M.T. Bodduluri, N. H. de Leeuw, S. Hansen, R. Adelung, Al2O3/ZnO composite-based sensors for battery safety applications: an experimental and theoretical investigation, Nano Energy 109 (2023) 108301.

[2] S. Zhai, X. Jiang, D. Wu, L. Chen, Y. Su, H. Cui, F. Wu, Single Rh atom decorated pristine and S-defected PdS2 monolayer for sensing thermal runaway gases in a lithium-ion battery: a first-principles study, Surf. Interfaces. 37 (2023) 102735.

[3] S. Guan, L. Tao, P. Tang, R. Fang, H. Wu, N. Piao, H. Yang, G. Hu, X. Geng, L. Li, B. An, F. Li, Regulating interfacial chemistry and kinetic behaviors of F/Mo co-doping Ni-rich layered oxide cathode for long-cycling lithium-ion batteries over −20°C–60°C, J. Energy Chem. 94 (2024) 449–457.

[4] S. Li, H. Zhang, L. Wu, H. Zhao, L. Tao, L. Li, C. Sun, D. Ju, B. An, An asymmetric electrode matching reversible kinetics of oxygen reaction for a rechargeable Zn-air battery, Chem. Eng. J. 482 (2024) 148868.

[5] H. Zhou, W. Han, H. Chai, H. Huang, J. Zheng, H. Zhang, L. Li, W. Zhou, B. An, C. Sun, Metal-ion exsolution effect to accelerate the reaction kinetics in Li–S batteries, J. Mater. Chem. A 12 (2024) 20238–20246.

[6] K. Nie, X. Wang, J. Qiu, Y. Wang, Q. Yang, J. Xu, X. Yu, H. Li, X. Huang, L. Chen, Increasing Poly(ethylene oxide) stability to 4.5 V by surface coating of the cathode, ACS. Energy Lett. 5 (2020) 826–832.

[7] M.H. Jung, M. Kwak, J. Ahn, J.Y. Song, H. Kang, H.T. Jung, Highly sensitive and selective acetylene CuO/ZnO Heterostructure sensors through electrospinning at lean O(2) concentration for transformer diagnosis, ACS. Sens. 9 (2024) 217–227.

[8] D. Chen, Y. Li, S. Xiao, C. Yang, J. Zhou, B. Xiao, Single Ni atom doped WS2 monolayer as sensing substrate for dissolved gases in transformer oil: a first-principles study, Appl. Surf. Sci. 579 (2022) 152141.

[9] H. Wang, H. Wu, H. Cui, Adsorption of H2 and C2H2 onto Rh-decorated InN monolayer and the effect of applied electric field, Mol. Phys/ (2022) 120.

[10] H. Zhang, Y. Zhang, L. Li, H. Zhou, M. Wang, L. Li, X. Geng, B. An, C. Sun, A rational design of titanium-based heterostructures as electrocatalyst for boosted conversion kinetics of polysulfides in Li-S batteries, J. Colloid Interface Sci. 633 (2023) 432–440.

[11] Y. Liu, M. Ren, B. Song, M. Dong, A DFT study of toxic gases (NH3, C2H2, NO) adsorption and detection on metal oxides (CuO, Ag2O, In2O3) modified MoTe2 monolayer, Appl. Surf. Sci. 622 (2023) 156858.

[12] A. Kumar, N. Sharma, A.P. Gutal, D. Kumar, P. Kumar, M. Paranjothy, M. Kumar, Growth and NO2 gas sensing mechanisms of vertically aligned 2D SnS2 flakes by CVD: experimental and DFT studies, Sensor. Actuator. B: Chem. 353 (2022) 131078.

[13] B. Mondal, X. Zhang, S. Kumar, F. Long, N.K. Katiyar, M. Kumar, S. Goel, K. Biswas, A resistance-driven H(2) gas sensor: high-entropy alloy nanoparticles decorated 2D MoS(2), Nanoscale, 15 (2023) 17097–17104.

[14] G. Liu, T. Chen, G. Zhou, Z. Xu, X. Xiao, Nonvolatile electrical control and reversible gas capture by ferroelectric polarization switching in 2D FeI(2)/In(2)S (3) van der waals heterostructures, ACS. Sens. 8 (2023) 1440–1449.

[15] J. Rehman, J. Gao, T. Yu, A. El-marghany, G. Yang, A novel 2D VC4 as a promising Na-host material for Na-ion batteries: computational insights, J. Mater. Chem. A 12 (2024) 6703–6711.

[16] H. Cui, M. Ran, X. Peng, G. Zhang, First-principles design of noble metal (Rh and Pd) dispersed Janus WSTe monolayer for toxic gas sensing applications, J. Environ. Chem. Eng. 12 (2024) 112047.

[17] L. Lin, Y. Sun, K. Xie, P. Shi, X. Yang, D. Wang, First-principles study on the catalytic performance of transition metal atom-doped CrSe 2 for the oxygen reduction reaction, Phys. Chem. Chem. Phys. 25 (2023) 15441–15451.

[18] S. Ma, D. Yuan, Z. Jiao, T. Wang, X. Dai, Monolayer Sc2CO2: a promising candidate as a SO2 gas sensor or capturer, J. Phys. Chem. C 121 (2017) 24077–24084.

[19] H.-Y. Zhuo, X. Yu, Q. Yu, H. Xiao, X. Zhang, J. Li, Selective hydrogenation of acetylene on graphene-supported non-noble metal single-atom catalysts, Sci. China Mater. 63 (2020) 1741–1749.

[20] D. Raval, S.K. Gupta, P.N. Gajjar, Janus PdSTe nanosheet as promising contender for detection of volatile organic compounds (VOCs) in human breath: a first principles investigation, Chem. Eng. J. 466 (2023) 143101.

[21] X. Li, X. Wu, Y. Zhao, Y. Lin, J. Zhao, C. Wu, H. Liu, L. Shan, L. Yang, L. Song, J. Jiang, Promoting oxygen reduction reaction by inducing out-of-plane polarization in a metal phthalocyanine catalyst, Adv. Mater. 35 (2023).

[22] K. Boonpalit, J. Kinchagawat, C. Prommin, S. Nutanong, S. Namuangruk, Efficient exploration of transition-metal decorated MXene for carbon monoxide sensing using integrated active learning and density functional theory, Phys. Chem. Chem. Phys. 25 (2023) 28657–28668.

[23] L. Lin, K. Xie, C. He, Nitrogen-vacancy-modulated efficient ammonia desorption over 3d TM-anchored BC 3 N 2 monolayer, Phys. Chem. Chem. Phys. 26 (2024) 2082–2092.

[24] Z. Yang, Z. Zhang, Y. Mu, C. Yue, Z. Liu, D. Dastan, X.-T. Yin, X. Ma, Improvement of gas sensitivity to ethanol by hydrothermal preparation of Dy-doped In2O3, Sensor. Actuator. B: Chem. 405 (2024) 135386.

[25] J. Choi, T. Kim, H. Li, H.T. Jung, D. Zhao, Gas sensors with two-dimensional rGO@ COF composite materials for fast NO(2) detection under room temperature, ACS Appl. Mater. Interfaces 15 (2023) 44119–44126.

[26] C. Anichini, W. Czepa, D. Pakulski, A. Aliprandi, A. Ciesielski, P. Samori, Chemical sensing with 2D materials, Chem. Soc. Rev. 47 (2018) 4860–4908.

[27] J. Hu, S. Zhai, Q. Zhang, H. Cui, X. Jiang, Two-dimensional HfTe2 monolayer treated by dispersed single Pt atom for hazardous gas Detection: a First-principles study, Appl. Surf. Sci. 605 (2022) 154572.

[28] X. Zheng, Y. Liu, Y. Yao, Trimetallic single-cluster catalysts for electrochemical nitrogen reduction reaction: activity prediction, mechanism, and electronic descriptor, Chem. Eng. J. 426 (2021) 130745.

[29] L. Cai, N. Zhang, B. Qiu, Y. Chai, Computational design of transition metal single-atom electrocatalysts on PtS2 for efficient nitrogen reduction, ACS Appl. Mater. Interfaces 12 (2020) 20448–20455.

[30] M. Wu, F. Dong, Y. Yang, X. Cui, X. Liu, Y. Zhu, D. Li, S. Omanovic, S. Sun, G. Zhang, Emerging atomically precise metal nanoclusters and ultrasmall nanoparticles for efficient electrochemical energy catalysis: synthesis strategies and surface/interface engineering, Electrochem. Energ. Rev. 7 (2024) 10.

[31] T. Jiang, C. Liu, C. Wang, H. Wu, M. Bi, X. Chen, J. He, Adsorption and sensing properties of dissolved gases in transformer oil using Cun and Pdn (n= 1–3) cluster doped WSe2 monolayers, Sensor. Actuator. A: Phys. 377 (2024) 115742.

[32] M. Bi, C. Xie, H. Wu, C. Liu, Z. Tong, Y. Du, T. Jiang, DFT insights into the TM (Cu, Ni, Ag) and TMO (CuO, NiO, Ag2O) modified HfSe2 for detecting PD fault gases, Comput. Theor. Chem. 1239 (2024) 114755.

[33] H. Cui, D. Chen, C. Yan, Y. Zhang, X. Zhang, Repairing the N-vacancy in an InN monolayer using NO molecules: a first-principles study, Nanoscale Adv. 1 (2019) 2003–2008.

[34] H.Y. Zhuo, X. Zhang, J.X. Liang, Q. Yu, H. Xiao, J. Li, Theoretical understandings of graphene-based metal single-atom catalysts: stability and catalytic performance, Chem. Rev. 120 (2020) 12315–12341.

[35] X. Li, G. Zhao, K. Xie, P. Wang, C. Zhang, L. Lin, Cu-decorated HfS2 and Cu-embedded HfS2 for adsorption and gas sensing of lithium-ion thermal runaway gases: a DFT study, Surf. Interfaces. 46 (2024) 104028.

[36] X. Wan, W. Yu, A. Wang, X. Wang, J. Robertson, Z. Zhang, Y. Guo, High-throughput screening of gas sensor materials for decomposition products of eco-friendly insulation medium by machine learning, ACS. Sens. 8 (2023) 2319–2330.

[37] S. Kang, M. Jeon, J. Kim, Density functional theory study of synergistic gas sensing using an electrically conductive mixed ligand two-dimensional metal–organic framework, ACS. Sens. 8 (2023) 3448–3457.

[38] S.J. Kim, Y.I. Kim, B. Lamichhane, Y.H. Kim, Y. Lee, C.R. Cho, M. Cheon, J.C. Kim, H.Y. Jeong, T. Ha, J. Kim, Y.H. Lee, S.G. Kim, Y.M. Kim, S.Y. Jeong, Flat-surface-assisted and self-regulated oxidation resistance of Cu(111), Nature 603 (2022) 434–438.

[39] F.-Y. Chiang, P.-H. Hsiao, T.-Y. Wu, V.K. Dien, M.-F. Lin, C.-Y. Chen, DFT and experimental interpretations of silicon-based room-temperature NO2 sensors improving humidity independence, Sensor. Actuator. B: Chem. 390 (2023) 133996.

[40] L. Li, H. Cao, Z. Liang, Y. Cheng, T. Yin, Z. Liu, S. Yan, S. Jia, L. Li, J. Wang, Y. Gao, First-principles study of Ti-Deficient Ti3C2 MXene nanosheets as NH3 gas sensors, ACS. Appl. Nano Mater. 5 (2022) 2470–2475.

[41] Z. Wang, R. Zhang, Z. Liu, X. Wei, M. Zhao, X. Zhang, Y. Yong, H. Cui, X. Li, C6N7 monolayer as an innovative sensor and scavenger for NO, H2S and SO2: a first-principles study, Surf. Interfaces. 39 (2023) 102971.

[42] Y. Zhao, D. Ma, J. Zhang, Z. Lu, Y. Wang, Transition metal embedded C3N monolayers as promising catalysts for the hydrogen evolution reaction, Phys. Chem. Chem. Phys. 21 (2019) 20432–20441.

[43] P. Wu, X. Zhang, D. Chen, J. Tang, Adsorption of SF6 decomposed products on ZnO-modified C3N: a theoretical study, Nanoscale Res. Lett 15 (2020) 186.

[44] Y. Liu, T. Shi, Q. Si, T. Liu, Adsorption and sensing performances of transition metal (Pd, Pt, Ag and Au) doped MoTe2 monolayer upon NO2: a DFT study, Phys. Lett. A 391 (2021) 127117.

[45] W. Nong, S. Qin, F. Huang, H. Liang, Z. Yang, C. Qi, Y. Li, C. Wang, Designing C3N-supported single atom catalysts for efficient nitrogen reduction based on descriptor of catalytic activity, Carbon N Y 182 (2021) 297–306.

[46] Y. Zhou, G. Gao, J. Kang, W. Chu, L.-W. Wang, Transition metal-embedded two-dimensional C3N as a highly active electrocatalyst for oxygen evolution and reduction reactions, J. Mater. Chem. A 7 (2019) 12050–12059.

[47] Z. Chen, J. Zhao, C.R. Cabrera, Z. Chen, Computational screening of efficient single-atom catalysts based on graphitic carbon nitride (g-C3N4) for nitrogen electroreduction, Small. Methods 3 (2018) 1800368.

[48] X. Wang, H. Niu, X. Wan, A. Wang, F.R. Wang, Y. Guo, Impact of coordination environment on single-atom-embedded C3N for oxygen electrocatalysis, ACS Sustain. Chem. Eng. 10 (2022) 7692–7701.

[49] J. Zhang, T. Xu, D. Yuan, J. Tian, D. Ma, CO2 electroreduction by transition metal-embedded two-dimensional C3N: a theoretical study, J. CO2 Utilizat. 43 (2021) 101367.

[50] M. Gu, L. Tao, D. Dastan, J. Dang, T. Fang, B. An, Metal-modified C3N1 monolayer sensors for battery instability monitoring, J. Mater. Chem. A 12 (2024) 15254–15264.

[51] X.-T. Yin, L. Tao, Fabrication and gas sensing properties of Au-loaded SnO2 composite nanoparticles for low concentration hydrogen, J. Alloys Compd. 727 (2017) 254–259.

[52] J. Zhang, L. Zhang, D. Leng, F. Ma, Z. Zhang, Y. Zhang, W. Wang, Q. Liang, J. Gao, H. Lu, Nanoscale Pd catalysts decorated WO3–SnO2 heterojunction nanotubes for highly sensitive and selective acetone sensing, Sensor. Actuator. B: Chem. 306 (2020) 127575.

[53] G. Pandey, M. Bhardwaj, S. Kumar, S.D. Lawaniya, M. Kumar, P.K. Dwivedi, K. Awasthi, Synergistic effects of Pd-Ag decoration on SnO/SnO2 nanosheets for enhanced hydrogen sensing, Sensor. Actuator. B: Chem. 402 (2024) 135062.

[54] B. Delley, From molecules to solids with the DMol3 approach, J. Chem. Phys. 113 (2000) 7756–7764.

[55] J.P. Perdew, K. Burke, M. Ernzerhof, Generalized gradient approximation made simple, Phys. Rev. Lett. 77 (1996) 3865–3868.

[56] J.P. Perdew, Y. Wang, Accurate and simple analytic representation of the electron-gas correlation energy, Phys. Rev. B, Condensed Matter 45 (1992) 13244–13249.

[57] S. Grimme, Semiempirical GGA-type density functional constructed with a long-range dispersion correction, J. Comput. Chem. 27 (2006) 1787–1799.

[58] R.S. Mulliken, Electronic Population Analysis on LCAO–MO molecular wave functions. I, J. Chem. Phys. 23 (1955) 1833–1840.

[59] M.I. Ahmed, L.J. Arachchige, Z. Su, D.B. Hibbert, C. Sun, C. Zhao, Nitrogenase-inspired atomically dispersed Fe–S–C linkages for improved electrochemical reduction of dinitrogen to ammonia, ACS Catal. 12 (2022) 1443–1451.

[60] L. Tao, J. Huang, D. Dastan, T. Wang, J. Li, X. Yin, Q. Wang, CO2 capture and separation on charge-modulated calcite, Appl. Surf. Sci. 530 (2020) 147265.

[61] Y. Sun, L. Tao, M. Wu, D. Dastan, J. Rehman, L. Li, B. An, Multi-atomic loaded C2N1 catalysts for CO2 reduction to CO or formic acid, Nanoscale 16 (2024) 9791–9801.

[62] M. Wang, W. Ma, C. Tan, Z. Qiu, L. Hu, X. Lv, Q. Li, J. Dang, Designing efficient non-precious metal electrocatalysts for high-performance hydrogen production: a comprehensive evaluation strategy, Small. (2023) e2306631.

[63] Z. Lv, W. Ma, M. Wang, J. Dang, K. Jian, D. Liu, D. Huang, Co-Constructing Interfaces of Multiheterostructure on MXene (Ti3C2Tx)-Modified 3D Self-Supporting Electrode for Ultraefficient Electrocatalytic HER in Alkaline Media, Adv. Function. Mater., 31 (2021) 2102576.

[64] L. Tao, D. Dastan, W. Wang, P. Poldorn, X. Meng, M. Wu, H. Zhao, H. Zhang, L. Li, B. An, Metal-decorated InN monolayer senses N2 against CO2, ACS Appl. Mater. Interfaces 15 (2023) 12534–12544.

[65] J. Li, C. Hou, C. Chen, W. Ma, Q. Li, L. Hu, X. Lv, J. Dang, Collaborative interface optimization strategy guided ultrafine RuCo and MXene heterostructure electrocatalysts for efficient overall water splitting, ACS Nano 17 (2023) 10947–10957.

[66] J. Li, C. Chen, Z. Lv, W. Ma, M. Wang, Q. Li, J. Dang, Constructing heterostructures of ZIF-67 derived C, N doped Co2P and Ti2VC2T MXene for enhanced OER, J. Mater. Sci. Technol. 145 (2023) 74–82.

[67] S. Nie, L. Tao, J. Li, W. Wang, P. Poldorn, Y. He, X. Yin, M. Wu, A single response to reducing gases by NiO-TiO2 heterojunction nanocrystals, Appl. Surf. Sci. 644 (2024) 158821.

[68] S. Nie, J. Li, L. Tao, Y. He, D. Dastan, X. Meng, P. Poldorn, X. Yin, Insights into selective mechanism of NiO-TiO2 Heterojunction to H2 and CO, ACS. Sens. 8 (2023) 4121–4131.

[69] L. Tao, J. Huang, X. Yin, Q. Wang, Z. Li, G. Wang, B. Cui, Adsorption kinetics of CO2 on a reconstructed calcite surface: an experiment-simulation collaborative method, Energy Fuels 33 (2019) 8946–8953.

[70] L. Tao, J. Huang, D. Dastan, J. Li, X. Yin, Q. Wang, Flue gas separation at organic-inorganic interface under geological conditions, Surf. Interfaces. 27 (2021) 101462.

[71] S. Liu, M. Ge, L. Meng, X. Liu, T. Fang, Mechanism analysis of CO2 separation from pvdf-supported deep eutectic solvent:a molecular dynamics simulation study, J. Mol. Liq. 403 (2024) 124806.